3D equilibrium shapes of periodically arranged anisotropic precipitates with elastic misfit

Dedicated to Professor Zenon Mróz
on the occasion of his 70th birthday

R. MUELLER, S. ECKERT and D. GROSS

Institute of Mechanics, Darmstadt University of Technology,
Hochschulstr. 1, D-64289 Darmstadt, Germany

A NUMERICAL PROCEDURE for simulating the equilibrium shapes of precipitates in two-phase materials, such as Ni-base alloys, is presented. Assuming a periodic arrangement of precipitates, a unit cell is analyzed to take particle interaction in 3D into account. Using the concept of generalized driving forces as the source of morphological evolution, a necessary condition for an equilibrium shape is derived. In the derivation of the driving force, elastic strain energy arising from the elastic misfit of the two phases and interface energy is considered. Both phases are assumed to be linear elastic but anisotropic and different from each other. The periodic cell problem is numerically solved by the Boundary Element Method. Numerical simulation for material parameters which mimic Ni-base alloys shows the influence of particle size, stiffness ratio of the two phases, volume fraction and external load on the resulting equilibrium shapes.

Key Words: Micromechanics, Eigenstrains, Anisotropic Boundary Element Method, Periodic Cell, Particle Interaction

1. Introduction

IN HIGH TEMPERATURE applications such as turbine blades, the Ni-base alloys are frequently used. Due to their superior mechanical and thermal properties they are also termed super-alloys. These single crystal materials possess in general a cuboidal microstructure of γ'-precipitates embedded in a Ni-matrix. The morphology on the micro-level strongly influences the mechanical and thermal material properties on the macro-level. Diffusion processes within the crystal lattice change the micromorphology at elevated temperatures and in the presence of stress fields. This phenomenon is called rafting and has been experimentally investigated for many years (see for example [1 – 4]). Due to their industrial importance, there has been a great effort of theoretical investigations of these two-phase materials, see for example [5 – 13]. Many of the theoretical investigations lead to numerical simulations which revealed the influence of certain

material parameters. In general, the modelling efforts of the microstructure can be divided into three groups:

– The first group of researchers treats the two-phase material via a Monte-Carlo simulation [14 – 18]. The different phases are identified by different "atoms" and generating a Boltzmann weighted chain of exchanges, the global energy minimum is found corresponding to an equilibrium configuration. This method is however very time-consuming and only a few 3D results have been published so far [19].

– In the second approach, a concentration or order parameter is introduced to distinguish the two phases. Often the assumption of elastically homogeneous phases is made to apply the method of Fast/Discrete Fourier Transforms (see for example [20 – 24]). The model requires the accurate resolution of very steep gradients. Therefore a very fine numerical grid is required. Due to the numerical effort only very few 3D results are known to the authors [25].

– In the third approach, which is pursued by the authors, the two-phase material is treated with a sharp interface model. The numerical implementation of this model can be done efficiently by using a Boundary Element Method [26 – 32]. In 3D, results were obtained for a fairly general set of material parameters [33, 34], however until now particle interaction has been neglected in 3D. With the periodic cell arrangement, this shortcoming is to be overcome and more realistic simulations are expected.

In the following, the periodic cell arrangement is taken as the first step to take particle interaction into account. From 2D calculations it is known that neighboring particles can disturb the stress field around a precipitate significantly [32] and therefore influence the equilibrium shape. The periodic arrangement is chosen for two reasons. Firstly due to its physical relevance, as many Ni-base alloys display a rather regular periodic microstructure, secondly for its efficient implementation of 3D interaction effects. In this context, it must be mentioned that, with the computational power available to the authors, a complex structure of more than two nonperiodically interacting 3D particles is at the moment not computable. On the other hand, the simulation of a periodic arrangement predicts the effect of the volume fraction of the precipitate phase on the micromorphology. This is generally believed to be an important factor [35 – 37] together with the particle size and the external loading situation.

2. Micromechanical model

2.1. Periodic unit cell model

Considered is a periodic arrangement of unit cells, each consisting of a particle $\mathcal{B}$ (γ'-phase) embedded in a matrix (γ-phase). The normal vector **n** points

from the interface ∂B into the matrix phase (see Fig. 1). The elastic properties of the precipitate and the matrix are assumed to be given by the elasticity tensors $\mathbb{C}^{in/out}$ respectively, which are allowed to be generally anisotropic. A possible lattice misfit between the γ'-phase and the matrix is taken into account by an inelastic eigenstrain ε^0 in the precipitate phase, which is assumed to be constant in the precipitate. Therefore the stress σ can be computed by Hooke's law in the two phases

$$(2.1) \qquad \sigma = \begin{cases} \mathbb{C}^{out}\varepsilon & \text{in the matrix phase,} \\ \mathbb{C}^{in}\left(\varepsilon - \varepsilon^0\right) & \text{in the precipitate phase,} \end{cases}$$

where ε is the linearized strain tensor. The interface ∂B between the precipitate and the matrix is perfectly coherent, thus the jump in the displacements $\mathbf{u}$ vanishes on the surface ∂B:

$$(2.2) \qquad [\![\mathbf{u}]\!] = \mathbf{0}, \quad \text{where} \quad [\![(\cdot)]\!] = (\cdot)^{out} - (\cdot)^{in}.$$

Periodic cell arrangement   Unit cell

$$\Gamma = \Gamma_1^+ \cup \Gamma_1^- \cup \Gamma_2^+ \cup \Gamma_2^- \cup \Gamma_3^+ \cup \Gamma_3^-$$
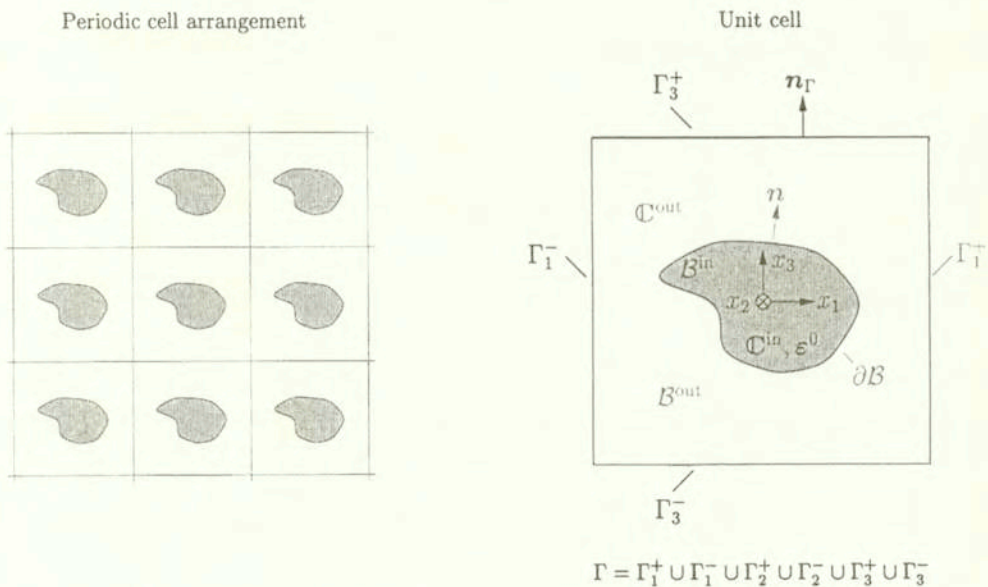
FIG. 1. Periodic arrangement of unit cells with precipitate.

On the exterior boundary of the cubic cell, the displacements $\mathbf{u}$ and tractions $\mathbf{t}$ have to satisfy periodicity conditions in order to ensure periodic filling of the entire material space. The cell boundary is denoted by Γ with its associated outward unit vector given by $\mathbf{n}_\Gamma$. The displacements $\mathbf{u}$ on two opposite cell boundaries $\Gamma_i^\pm$ (see Fig. 1) satisfy

$$(2.3) \qquad \mathbf{u}|_{\Gamma_i^+} - \mathbf{u}|_{\Gamma_i^-} = \mathbf{v}_i \quad \text{for } i = 1, 2, 3,$$

where the three vectors $\mathbf{v}_i$ are still undetermined translations. The periodicity conditions for the tractions are given by the following set of equations:

$$(2.4) \qquad \mathbf{t}|_{\Gamma_i^+} + \mathbf{t}|_{\Gamma_i^-} = \mathbf{0} \quad \text{for} \quad i = 1, 2, 3.$$

In the absence of external loads, the mechanical equilibrium of the periodic cell arrangement leads to three vector equations

$$(2.5) \qquad \int_{\Gamma_i^+} \mathbf{t}\, dA = \mathbf{0} \quad \text{for} \quad i = 1, 2, 3$$

to determine the unknown translations $\mathbf{v}_i$. Equation (2.5) needs to be modified in the case of an external load σ^∞. However with the use of an equivalent eigenstrain

$$(2.6) \qquad \varepsilon_{\text{eq}}^0 = \varepsilon^0 - [\![\mathbb{C}^{-1}]\!]\sigma^\infty$$

instead of the physical eigenstrains ε^0, Eqs. (2.1) – (2.5) can still be used. A detailed discussion of equivalent eigenstrain is given in [38, 39].

2.2. Variational principle and equilibrium conditions

In the absence of external loads, the total potential of the system is given by the sum of the elastic strain energy

$$(2.7) \qquad E^{\text{el}} = \int_{\mathcal{B}^{\text{in}}} W\, dV + \int_{\mathcal{B}^{\text{out}}} W\, dV, \quad \text{where} \quad W = \frac{1}{2}\sigma : \varepsilon^{\text{el}}$$

and the interface energy

$$(2.8) \qquad E^{\text{int}} = \gamma_{\text{s}} \int_{\partial \mathcal{B}} dA.$$

Here the interface energy is assumed to be given by a constant interface energy density γ_{s}. For coherent interfaces the assumption of constant interface energy density is a good approximation (see [26, 28, 29], and related works for details and values of γ_{s}). In [27] the authors discuss the possibility of determining γ_{s} inversely by comparing experimental results with the simulated behaviour. Mass conservation dictates that the particle volume

$$(2.9) \qquad V_{\mathcal{B}} = \int_{\mathcal{B}^{\text{in}}} dV = V_0$$

remains constant V_0. Equilibrium is defined by extremizing the total potential for a given particle size V_0. This constraint is expressed by an augmented Lagrange functional

$$(2.10) \qquad \tilde{E}(\mathbf{u}, \partial \mathcal{B}, \lambda) = E^{\text{el}} + E^{\text{int}} + \lambda\,(V_{\mathcal{B}} - V_0)\,,$$

with the Lagrange multiplier λ. Applying calculus of variations with respect to the displacement field $\mathbf{u}$, the morphology $\partial \mathcal{B}$ and the Lagrange multiplier λ leads to

$$(2.11) \qquad \delta \tilde{E} = \int_{\mathcal{B}^{\text{in}}} \delta W \, dV + \int_{\mathcal{B}^{\text{out}}} \delta W \, dV - \int_{\partial \mathcal{B}} (\llbracket W \rrbracket + \kappa \gamma_{\text{s}} - \lambda) \, \delta n \, dA$$

$$+ \delta \lambda \, (V_{\mathcal{B}} - V_0) = 0,$$

where δn is the morphological variation of the interface $\partial \mathcal{B}$ in the normal direction and κ denotes twice the mean curvature (taken to be negative for a sphere) regarding the change of interface area. Applying the divergence theorem to the precipitate and matrix phase yields

$$(2.12) \qquad \delta \tilde{E} = - \int_{\mathcal{B}^{\text{in}}} \text{div} \boldsymbol{\sigma} \cdot \delta \mathbf{u} \, dV - \int_{\mathcal{B}^{\text{out}}} \text{div} \boldsymbol{\sigma} \cdot \delta \mathbf{u} \, dV + \underbrace{\int_{\Gamma} \boldsymbol{\sigma} \mathbf{n}_{\Gamma} \cdot \delta \mathbf{u} \, dA}_{I}$$

$$- \int_{\partial \mathcal{B}} \underbrace{\llbracket \boldsymbol{\sigma} \mathbf{n} \cdot \delta \mathbf{u} \rrbracket}_{\mathit{II}} \, dA - \int_{\partial \mathcal{B}} (\llbracket W \rrbracket + \gamma_{\text{s}} \kappa - \lambda) \, \delta n \, dA + \delta \lambda \, (V_{\mathcal{B}} - V_0) = 0,$$

where the integral I over Γ vanishes on account of (2.3) and (2.4). The jump term II can further be simplified by the help of

$$(2.13) \qquad \llbracket ab \rrbracket = \langle a \rangle \llbracket b \rrbracket + \llbracket a \rrbracket \langle b \rangle, \quad \text{where} \quad \langle (\cdot) \rangle = \frac{1}{2} \left((\cdot)^{\text{out}} + (\cdot)^{\text{in}} \right),$$

therefore leading to

$$(2.14) \qquad \mathit{II} = \llbracket \boldsymbol{\sigma} \mathbf{n} \cdot \delta \mathbf{u} \rrbracket = \langle \boldsymbol{\sigma} \mathbf{n} \rangle \cdot \llbracket \delta \mathbf{u} \rrbracket + \llbracket \boldsymbol{\sigma} \mathbf{n} \rrbracket \cdot \langle \delta \mathbf{u} \rangle.$$

As a consequence of the coherency condition (2.2), the jump of the displacement variation is given by

$$(2.15) \qquad \llbracket \delta \mathbf{u} \rrbracket = - \llbracket \nabla \mathbf{u} \rrbracket \mathbf{n} \, \delta n,$$

which follows from the Lemma of Hadamard, (see [9] for details). Also note that $\llbracket \boldsymbol{\sigma} \mathbf{n} \rrbracket = \llbracket \boldsymbol{\sigma} \rrbracket \mathbf{n}$, thus Eq. (2.12) can be rewritten as

$$(2.16) \qquad \delta \tilde{E} = - \int_{\mathcal{B}^{\text{in}}} \text{div} \boldsymbol{\sigma} \cdot \delta \mathbf{u} \, dV - \int_{\mathcal{B}^{\text{out}}} \text{div} \boldsymbol{\sigma} \cdot \delta \mathbf{u} \, dV - \int_{\partial \mathcal{B}} \llbracket \boldsymbol{\sigma} \rrbracket \mathbf{n} \cdot \langle \delta \mathbf{u} \rangle \, dA$$

$$- \int_{\partial \mathcal{B}} (\llbracket W \rrbracket - \llbracket \nabla \mathbf{u} \rrbracket \mathbf{n} \cdot \langle \boldsymbol{\sigma} \mathbf{n} \rangle + \kappa \gamma_{\text{s}} - \lambda) \, \delta n \, dA + \delta \lambda \, (V_{\mathcal{B}} - V_0) = 0.$$

For arbitrary and admissible variations $\delta \mathbf{u}$, δn and $\delta \lambda$, the following conclusions can be drawn:

(i) Mechanical equilibrium in the bulk phases:

$$(2.17) \qquad \qquad \mathrm{div}\,\sigma = 0 \quad \text{in } \mathcal{B}^{\mathrm{in}} \text{ and } \mathcal{B}^{\mathrm{out}}.$$

(ii) Mechanical equilibrium on the interface:

$$(2.18) \qquad \qquad [\![\sigma]\!]\mathbf{n} = 0 \quad \text{on } \partial\mathcal{B}.$$

(iii) Morphological equilibrium condition:
(Note that (2.18) has been used to deduce that $\langle \sigma \mathbf{n} \rangle = \sigma \mathbf{n}$)

$$(2.19) \qquad \tau_{\mathrm{n}} = [\![W]\!] - \mathbf{n} \cdot \left([\![\nabla\mathbf{u}]\!]^{\mathrm{T}}\sigma\right)\mathbf{n} + \kappa\gamma_{\mathrm{s}} = \lambda \quad \text{on } \partial\mathcal{B}.$$

(iv) Volume constraint:

$$(2.20) \qquad \qquad V_{\mathcal{B}} = V_0.$$

In the following, mechanical equilibria (2.17) and (2.18) will be assumed to be satisfied. The remaining morphological variation δ_{m} with respect to the shape and the Lagrange parameter is

$$(2.21) \qquad \delta_{\mathrm{m}}\tilde{E} = -\int_{\partial\mathcal{B}} (\tau_{\mathrm{n}} - \lambda)\,\delta n\,dA + \delta\lambda\,(V_{\mathcal{B}} - V_0) = 0.$$

The driving force τ_{n} in the morphological equilibrium (2.21) can be related to Eshelby's concept of a force on an interface [40]. Writing

$$(2.22) \qquad \tau_{\mathrm{n}} = \mathbf{n} \cdot [\![\mathbf{P}]\!]\mathbf{n} + \gamma_{\mathrm{s}}\kappa, \quad \text{where} \quad \mathbf{P} = W\mathbf{1} - (\nabla\mathbf{u})^{\mathrm{T}}\sigma$$

with $\mathbf{P}$ being the energy-momentum tensor as defined by Eshelby, this identity is obvious. It is mentioned here that τ_{n} can be regarded as a configurational force using the terminology of Gurtin [9]. In the considered inclusion problem, the generalized driving force τ_{n} can be expressed by the strains ε on the inner side of the interface (see [30])

$$(2.23) \qquad \tau_{\mathrm{n}} = -\frac{1}{2}\left[\left(\mathbb{C}^{\mathrm{in}}\varepsilon^0 + [\![\mathbb{C}]\!]\varepsilon\right)\mathbf{n}\right] \cdot \Omega^{-1}\left[\left(\mathbb{C}^{\mathrm{in}}\varepsilon^0 + [\![\mathbb{C}]\!]\varepsilon\right)\mathbf{n}\right]$$

$$+ \frac{1}{2}\varepsilon : \mathbb{C}^{\mathrm{out}}\varepsilon - \frac{1}{2}\left(\varepsilon - \varepsilon^0\right) : \mathbb{C}^{\mathrm{in}}\left(\varepsilon - \varepsilon^0\right) + \gamma_{\mathrm{s}}\kappa,$$

where the components of the acoustic tensor Ω of the matrix material are given by

$$(2.24) \qquad \qquad \Omega_{ik} = \mathbb{C}^{\mathrm{out}}_{ijkl}n_j n_l.$$

The computation of τ_{n} requires the solution of the inhomogeneous inclusion problem. In Sec. 3 the solution procedure by a Boundary Element Method is

explained. It should be emphasized, that the computation of the driving force on the interface is independent of the specific arrangement of particles, because only local quantities are involved. The effect of a periodic arrangement enters the calculation of the driving force only through the solution of the elastic field problem, namely through the value of the strains ε.

Equation (2.19) is a necessary condition for a shape to be in morphological equilibrium, however it must be mentioned that this condition is not sufficient. This issue is discussed for example in [41 – 43] on the basis of analytical investigation, and numerical simulations in [27, 31] confirm this result. In order to perform the variation (2.21) in an algorithmic setting, the shape of the inclusion is given by a set of $q_1, \ldots, q_M$ shape parameters. These shape parameters can be a general description of the interface $\partial \mathcal{B}$, but in the calculation they coincide with the distance of the Boundary Element nodes from the origin of the coordinate system. This choice of shape parameters proved to be fairly general, as it covers the range from spheroids to cuboids, which are experimentally observed. Expressing the normal variation δn in (2.21) by variations of the shape parameters $\delta q_1, \ldots, \delta q_M$ leads to a nonlinear system of equations

$$
\begin{aligned}
F_1\left(q_1, \ldots, q_M, \lambda\right) &= -\int_{\partial \mathcal{B}}\left(\tau_n-\lambda\right) \frac{\partial \mathbf{x}}{\partial q_1} \cdot \mathbf{n}\, dA &= 0, \\
&\ \ \vdots &\ \ \vdots &\ \ \vdots \\
F_M\left(q_1, \ldots, q_M, \lambda\right) &= -\int_{\partial \mathcal{B}}\left(\tau_n-\lambda\right) \frac{\partial \mathbf{x}}{\partial q_M} \cdot \mathbf{n}\, dA &= 0, \\
F_{M+1}\left(q_1, \ldots, q_M, \lambda\right) &= V_{\mathcal{B}}-V_0 &= 0.
\end{aligned}
$$

(2.25)

Here the terms $F_1, \ldots, F_M$ are the work conjugated quantities of the respective shape parameters $q_1, \ldots, q_M$. This system of $M+1$ nonlinear equations for M shape parameters and the Lagrange multiplier λ is solved using a quasi-Newton solver. For details in the solution procedure, the reader is referred to [44]. The general setting is equivalent to that of a shape optimization with a geometrical constraint, i.e. constant particle volume. In the terminology of optimization the total potential of the system is the target function.

3. Boundary Integral Equation Method

The solution of the inhomogeneous inclusion problem can be found by applying the Boundary Integral Equation of elastostatics, which is discretized by Boundary Elements. It is a natural choice for the boundary variations considered here. The advantage of this method is, that the unknowns are shifted from the interior of the considered domain to its boundary, which reduces the problem

dimension and size. The standard integral equation for linear elastic problems follows from [45] to be

$$
(3.1) \qquad \mathbf{K}(\mathbf{x})\mathbf{u}(\mathbf{x}) + \int_A \mathbf{T}(\mathbf{x} - \mathbf{y})\mathbf{u}(\mathbf{y})\, dA = \int_A \mathbf{U}(\mathbf{x} - \mathbf{y})\mathbf{t}(\mathbf{y})\, dA,
$$

with $\mathbf{x}$ representing the source point and $\mathbf{y}$ the observation point, as well as $\mathbf{K} = \dfrac{1}{2}\mathbf{1}$ for a smooth surface. The fundamental solutions for the tractions and the displacements are expressed through $\mathbf{T}$ and $\mathbf{U}$ respectively.

3.1. Anisotropic fundamental solution

Since the lattice structure of the different phases in general shows anisotropic behaviour, the analytic fundamental solution for the isotropic case, known as the Kelvin problem, cannot be applied. A method to calculate these quantities numerically is proposed by [46] and incorporated to handle anisotropic behaviour. According to [46], the fundamental solution for the displacements can be expressed as follows

$$
(3.2) \qquad \mathbf{U} = \frac{1}{8\pi^2|\mathbf{x} - \mathbf{y}|}\mathbf{G}(\theta_1, \theta_2),
$$

with the kernel

$$
(3.3) \qquad \mathbf{G}(\theta_1, \theta_2) = \int_0^{2\pi} \mathbf{M}^{-1}(\mathbf{z}(\varphi))\, d\varphi
$$

and the argument of the integral

$$
(3.4) \qquad M_{ik} = \mathbb{C}_{ijkl}z_j z_l \qquad |\mathbf{z}| = 1.
$$
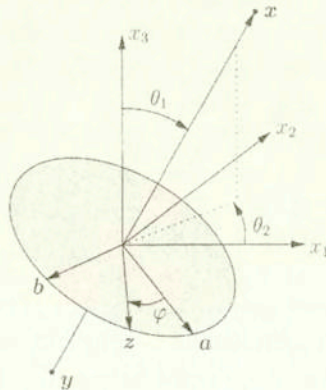
Fig. 2. Anisotropic fundamental solution.

Figure 2 provides a geometric representation of the quantities in Eq. (3.3). The function $\mathbf{G}(\theta_1, \theta_2)$ depends on the orientation of the vector $\mathbf{y} - \mathbf{x}$ but not on its length. Since $\mathbf{G}$ is a smooth function, discrete values for the domain $0 \leq \theta_1 \leq \pi$ and $0 \leq \theta_2 \leq 2\pi$ can be calculated. Instead of performing the integration in Eq. (3.3) for every pair $(\mathbf{x}, \mathbf{y})$ appearing in the problem, quadratic interpolation between the discrete values for the angles θ_1 and θ_2 is utilized. This approach increases the computational speed when integrating the Boundary Integral Equations. A similar procedure can be used to find the fundamental solution for the tractions and is described in [46].

3.2. Boundary Integral Equations

Applying the boundary element method to the problem of periodically arranged precipitates leads to two distinct problems for the matrix- and the particle-phase. Incorporating the jump Eqs. (2.2) and (2.18), the displacement- and the traction-vector are defined as

(3.5)
$$\mathbf{u}^{\mathrm{in}} = \mathbf{u}^{\mathrm{out}} = \mathbf{u} \qquad \text{on} \quad \partial \mathcal{B}$$

and

(3.6)
$$-\mathbf{t}^{\mathrm{out}} = \mathbf{t}^{\mathrm{in}} = \mathbf{t} \qquad \text{on} \quad \partial \mathcal{B}.$$

Following the general procedure, derivation of the boundary integral equations proposed by [45] yields three integral equations, two for the matrix boundaries $\partial \mathcal{B}$ and Γ and one for the particle boundary $\partial \mathcal{B}$:

(3.7)
$$\mathbf{K}^{\mathrm{out}}\, \mathbf{u} - \int_{\partial \mathcal{B}} \mathbf{T}^{\mathrm{out}}\, \mathbf{u}\, dA + \int_{\Gamma} \mathbf{T}^{\mathrm{out}}\, \mathbf{u}^{\Gamma}\, dA$$
$$+ \int_{\partial \mathcal{B}} \mathbf{U}^{\mathrm{out}}\, \mathbf{t}\, dA - \int_{\Gamma} \mathbf{U}^{\mathrm{out}}\, \mathbf{t}^{\Gamma}\, dA = 0 \qquad \text{on} \quad \partial \mathcal{B},$$

(3.8)
$$\mathbf{K}^{\Gamma}\, \mathbf{u}^{\Gamma} - \int_{\partial \mathcal{B}} \mathbf{T}^{\mathrm{out}}\, \mathbf{u}\, dA + \int_{\Gamma} \mathbf{T}^{\mathrm{out}}\, \mathbf{u}^{\Gamma}\, dA$$
$$+ \int_{\partial \mathcal{B}} \mathbf{U}^{\mathrm{out}}\, \mathbf{t}\, dA - \int_{\Gamma} \mathbf{U}^{\mathrm{out}}\, \mathbf{t}^{\Gamma}\, dA = 0 \qquad \text{on} \quad \Gamma,$$

(3.9)
$$\mathbf{K}^{\mathrm{in}}\, \mathbf{u} + \int_{\partial \mathcal{B}} \mathbf{T}^{\mathrm{in}}\, \mathbf{u}\, dA - \int_{\partial \mathcal{B}} \mathbf{U}^{\mathrm{in}}\, \mathbf{t}\, dA = \mathbf{K}^{\mathrm{in}}\, \mathbf{u}^0 + \int_{\partial \mathcal{B}} \mathbf{T}^{\mathrm{in}}\, \mathbf{u}^0\, dA \qquad \text{on} \quad \partial \mathcal{B}.$$

To achieve a complete system of equations, the periodicity conditions (2.3), (2.4) as well as the traction boundary condition for the unit cell (2.5) have to be considered. The integral equations are then discretized using 4-node elements with a bilinear interpolation of displacements, tractions and geometry. The discretization leads to a non-symmetric linear system of equations for the displacements and tractions on the interface and on the cell boundary. In the calculation of equilibrium shapes, the following discretization has been used:

	Number of nodes	Number of elements
Cell boundary Γ	218	216
Particle boundary ∂B	866	864

This system has to be solved repeatedly with a new particle geometry in the optimization process. About 25 – 50 iterations are needed in the quasi-Newtonian process to obtain the convergence.

4. Results

4.1. Nondimensionalization

For the numerical implementation of the problem it is useful to scale the different quantities in an appropriate way. This increases the numerical efficiency. According to [33], the following positive scalars are defined for the 3D case:

$$(4.1) \qquad l^* = \sqrt[3]{V_B},$$

$$(4.2) \qquad \varepsilon^* = \max_{i=1,2,3} |\varepsilon_i^0|,$$

$$(4.3) \qquad \mu^* = \frac{1}{15} \left[c_{11}^{\text{out}} + c_{22}^{\text{out}} + c_{33}^{\text{out}} - c_{12}^{\text{out}} - c_{23}^{\text{out}} - c_{13}^{\text{out}} + 3 \left(c_{44}^{\text{out}} + c_{55}^{\text{out}} + c_{66}^{\text{out}} \right) \right].$$

The characteristic length of the particle l^* is defined by the particle volume, and ε^* describes the maximal absolute value of the eigenstrains. The effective shear modulus μ^* characterizes the average stiffness of the anisotropic matrix material, here given by its Voigt constants. Following the procedure used in [31], a dimensionless formulation for all quantities of the system can be derived in conjunction with the dimensionless particle size

$$(4.4) \qquad L = \frac{\mu^* \varepsilon^{*2} l^*}{\gamma_s}.$$

Since L can be regarded as the ratio of the systems elastic strain energy E^{el} to the interfacial energy E^{int}, a physical interpretation is possible. If E^{int} approaches zero, L becomes very large and the particle shape is determined by the minimum of the elastic strain energy. In contrast, for a small value of L the influence of E^{int} is dominating, which leads to a sphere as an equilibrium morphology.

4.2. Verification

To check correctness and accuracy of the computations, the numerical results have to be compared with analytic solutions. However, if considering periodic arrangements of anisotropic misfitting particles, no analytic solution exists. To justify the calculations, some tests as well as comparison with 2D results were performed. For the test simulations the elastic behaviour is assumed to be isotropic for both phases with the material parameters

$$(4.5) \qquad \nu^{\mathrm{in}} = \nu^{\mathrm{out}} = 0.25, \quad \frac{\mu^{\mathrm{in}}}{\mu^{\mathrm{out}}} = \frac{1}{2},$$

where $\nu^{\mathrm{in/out}}$ is Poisson's constant and $\mu^{\mathrm{in/out}}$ denotes the corresponding shear modulus. Positive eigenstrains

$$(4.6) \qquad \varepsilon^0 = \varepsilon^* \mathbf{1} \quad \text{with} \quad \varepsilon^* = 0.001$$

are applied and the volume fraction f of the inclusion compared to the total volume is assumed to be

$$(4.7) \qquad f = \frac{V_{\mathcal{B}^{\mathrm{in}}}}{V_{\mathcal{B}^{\mathrm{tot}}}} = 12.5\%.$$

In the first calculation, the inclusion is shifted off the matrix center towards one face of Γ to control the assembling of the system matrix for nonsymmetric problems. Such a shift should not alter the stress distribution. For the dimensionless particle size $L = 6$ is chosen. As Fig. 3 shows, the stresses are repeated periodically on the matrix boundary for the symmetric as well as for the nonsymmetric problem.

0.223456
0.115989
0.0085233
−0.0989428
−0.206409
−0.313875
−0.421341
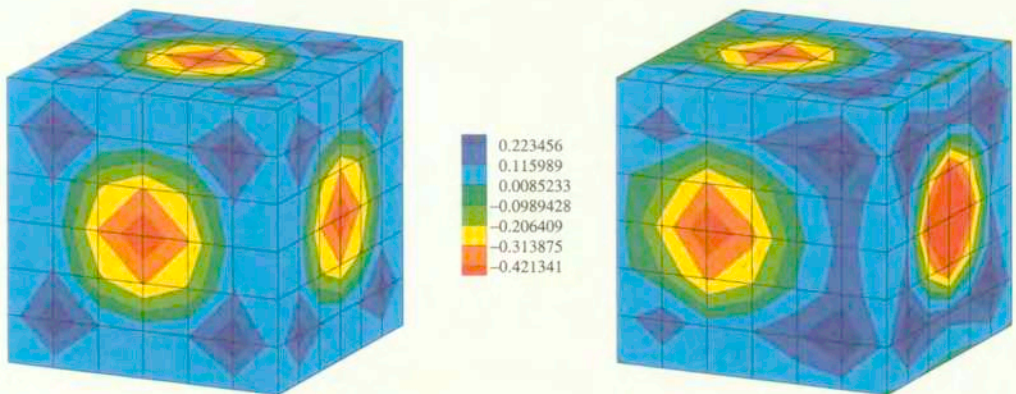
FIG. 3. Resolved normal stresses on the matrix boundary for shifted particle.

For the second test, demonstrating the influence of the matrix boundary to the radial strains on the interface, a value $L = 3$ is assumed. If sufficiently small volume fractions are considered, the periodic arrangement is assumed to have a negligible influence on the inclusion. Thus for $f \to 0$ the strains on the interface are expected to converge to the corresponding values for the single inclusion problem. Assuming isotropic material behaviour, this problem can be treated exactly and is known as Eshelby's solution. The difference in the radial strains is given by

$$(4.8) \qquad \Delta\varepsilon = \frac{\varepsilon - \varepsilon^\infty}{\varepsilon^\infty},$$

where ε^∞ denotes the reference strains for the single inclusion problem, and ε are the radial strains for periodic arrangement. Figure 4 shows the position of three different points (P_1, P_2, P_3) on the particle surface, for which the deviation is calculated. On all three points the radial strains show the same qualitative behaviour, for decreasing volume fraction the difference $\Delta\varepsilon$ also decreases and approaches zero for $f \to 0$.

$P_1 - P_3$ on $\partial\mathcal{B}$ $\qquad\qquad$ $\Delta\varepsilon$ for $P_1 - P_3$
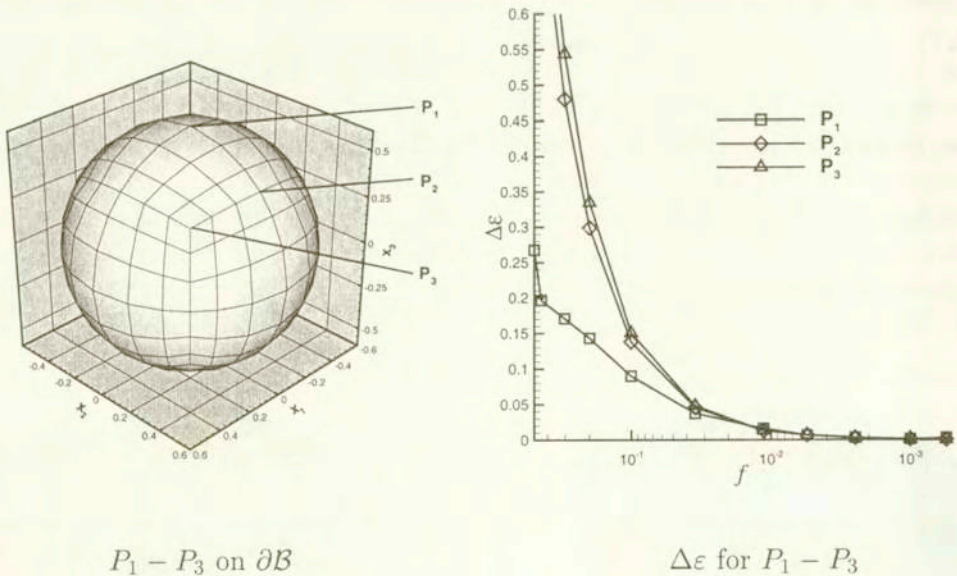
FIG. 4. Difference in radial strains as a function of f.

4.3. Equilibrium shapes

In this section the influence of different parameters on the equilibrium morphology will be discussed. In order to mimic the mechanical behaviour of Ni-base alloys, the elastic constants of Nickel in Voigt notation are used (see [47]):

$$(4.9) \quad \mathbb{C}^{\text{in}} = \mathbb{C}^{\text{out}} = \begin{pmatrix} 2.465 & 1.473 & 1.473 & 0 & 0 & 0 \\ 1.473 & 2.465 & 1.473 & 0 & 0 & 0 \\ 1.473 & 1.473 & 2.465 & 0 & 0 & 0 \\ 0 & 0 & 0 & 1.247 & 0 & 0 \\ 0 & 0 & 0 & 0 & 1.247 & 0 \\ 0 & 0 & 0 & 0 & 0 & 1.247 \end{pmatrix} \cdot 10^5 \frac{\text{N}}{\text{mm}^2}.$$

A dilatational eigenstrain tensor as given in Eq (4.6) is assumed. Due to the fcc-lattice structure, the elastic properties show cubic orthotropy. To visualize the elastic behaviour Fig. 5 shows a 3D representation of the directional Young's modulus. The material possesses a high stiffness along the diagonal direction, whereas along the coordinate axis Young's modulus is lower.
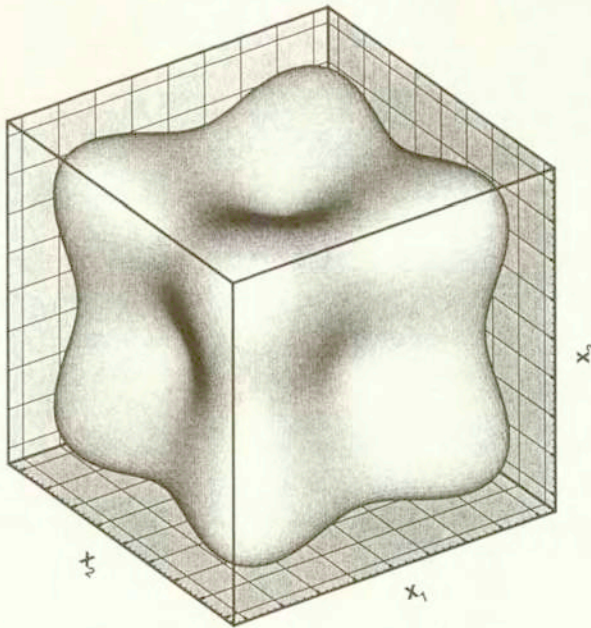
FIG. 5. Directional Young's modulus of material as given in (4.9).

As the computations are quite time-consuming and a lot of parameters influence the equilibrium shape, attention will be restricted to some basic parameters, such as volume fraction, particle size, stiffness ratio of particle to matrix material and loading. Of special interest is the influence of the volume fraction f and the particle interaction in 3D. However, these are only the first results that cannot cover the complete relevant parameter range.

4.3.1. Resolved normal stresses on the cell boundary. Before considering particle morphologies, the importance of the volume fraction f to the normal tractions on the cell boundary is discussed. In Fig. 6 negative normal tractions for $f = 50\%$ can be found at the center of each matrix face, while in the vicinity of the edges positive values appear. This is evident because the matrix material is under compression in the region where the interface of two adjoining particles are close together and leads to a convex cell shape if the assumption of a periodic arrangement is neglected.

| 0.31627 |
| 0.251254 |
| 0.186238 |
| 0.121222 |
| 0.0562058 |
| −0.00881028 |
| −0.0738264 |
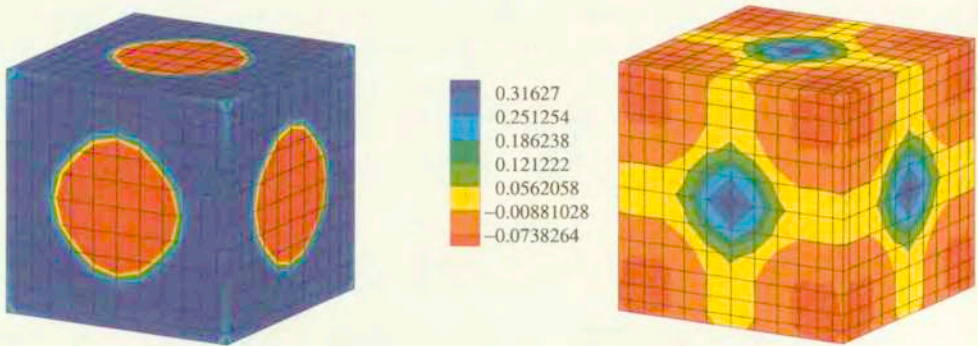
FIG. 6. Resolved normal stresses on the matrix boundary for different volume fractions.

Considering small volume fractions, Fig. 6 shows that the distribution of the normal stresses has changed. For $f = 10\%$ the positive tractions appear in the center, while at the edges negative values can be found. To explain that, the material behaviour due to orthotropy must be recalled. As a consequence of the high stiffness in the diagonal direction, the displacements on the interface along the diagonals are basically translated to the corners of the matrix boundary, leading to a concave deformation of the unit cell. To satisfy the conditions for periodically arranged particles, positive tractions have to be applied in the center of each face of Γ.

4.3.2. Influence of particle size and volume fraction. In the following, the influence of the particle size L as well as the importance of the volume fraction f will be discussed assuming the same elasticity tensor in the matrix and particle. In order to characterize the particle shape,

$$(4.10) \qquad \eta = \frac{d}{l}$$

is introduced (see Fig. 7). For $\eta = 1$, the shape is a sphere. A value of $\eta = \sqrt{3}$ characterizes a cube. Figure 7 shows the equilibrium shapes for different

combinations of the two parameters. The particle becomes cuboidal if L increases, independent of f. Recalling that L denotes the ratio of elastic to interface energy, this can be understood. A large particle minimizes the elastic energy by orienting large parts of the interface normal to the soft directions of the material - here normal to the coordinate axis. The interface energy is less dominant at large sizes, thus it rounds off only small regions at the edges and corners to cube-like shapes.
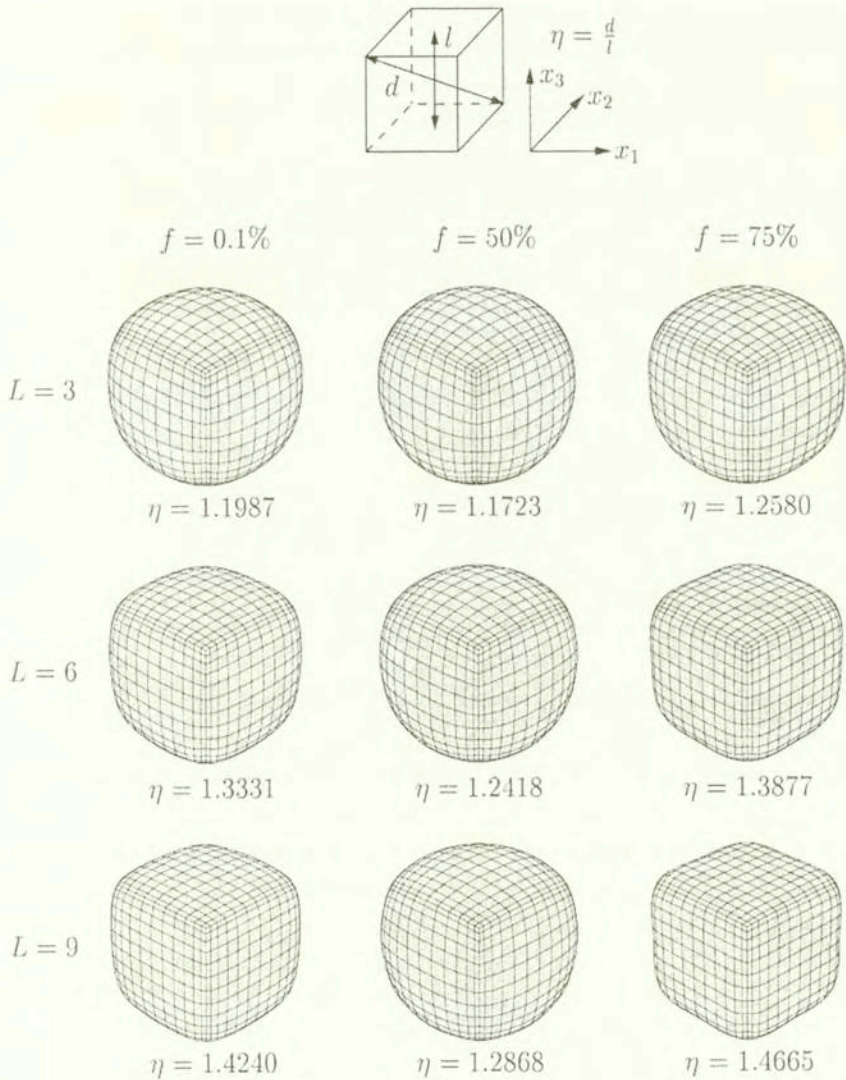
FIG. 7. Equilibrium shapes for different values of L and f.

When keeping the particle size L constant and increasing the volume fraction f, the particle first tends to a more sphere-like morphology but for even higher values of f, the particle looks more cuboidal. To give an explanation, the two components $E^{el,in}$ and $E^{el,out}$ contributing to the total elastic strain energy have to be considered. For increasing f, the value of $E^{el,out}$ decreases, so that the contribution of E^{el} to the total energy also decreases and the particle tends to a more sphere-like shape. This effect is relevant for volume fractions f of about 40 – 50%. Increasing the volume fraction further the particle shape becomes cube-like again, due to the geometrical constraint. A cube-like shape is the only way to place more particle material inside the periodic unit cell. The qualitative behaviour of the equilibrium shapes due to the variation of the parameters L and f agrees with the 2D results of [31].
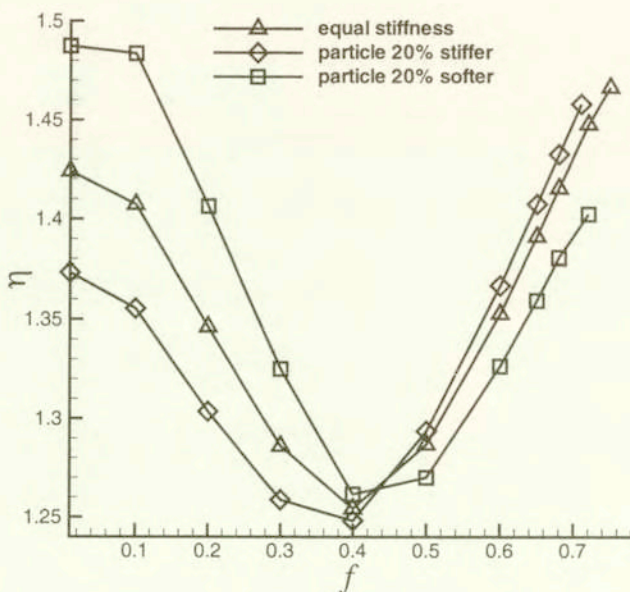
Fig. 8. Shape parameter ν as a function of f for different stiffness ratios.

4.3.3. *Influence of particle stiffness.* It is known from experimental observations and numerical simulations that the stiffness ratio of particle to matrix material is of great importance. In Fig. 8 the shape parameter η is plotted as a function of the volume fraction f for the stiffness ratio $\mathbb{C}^{in} = 0.8\,\mathbb{C}^{out}$, $\mathbb{C}^{in} = \mathbb{C}^{out}$ and $\mathbb{C}^{in} = 1.2\,\mathbb{C}^{out}$. The particle size is assumed to be $L = 9$. Comparing the three stiffness ratios, the soft particle is more cube-like than the stiff inclusion as long as the volume fraction f is small, whereas for large volume fractions f the stiff particle is more cuboidal than the soft inclusion. This behaviour is also found in [31] for the 2D case. All three stiffness ratios reach a minimal value of

the parameter η for volume fractions of $40-50\%$. For large volume fractions f, the particle shape is mostly determined by the material parameters of the inclusion. So a stiff particle leads to higher values of $E^{\text{el,in}}$ from which the cuboidal shape follows. When considering small volume fractions, the matrix material determines the equilibrium morphology. If the particle is assumed to exhibit stiff behaviour, the matrix material is comparatively soft and as a consequence, the inclusion shape looks more sphere-like.

4.3.4. *Influence of an applied load.* In the last example, the influence of an applied load on the equilibrium shape is considered for increasing volume fractions. The elasticity tensors are chosen to be $\mathbb{C}^{\text{in}} = 0.8\,\mathbb{C}^{\text{out}}$ and $L = 3$, the remote stress field $\sigma_{11}^{\infty} = 50\,\dfrac{\text{N}}{\text{mm}^2}$ is applied. To describe the particle shape, the quantity

$$(4.11) \qquad\qquad \rho = \frac{a-b}{a+b}$$

is introduced, where a and b define the principal axis of an oblate cuboid (see Fig. 9). If $a = b$, the parameter ρ equals zero, describing the particle shape with cubic symmetry, whereas for values $0 < \rho < 1$ an oblate shape is achieved.

$f = 0.1\%$ $\qquad\qquad$ $f = 24\%$ $\qquad\qquad$ $f = 36\%$
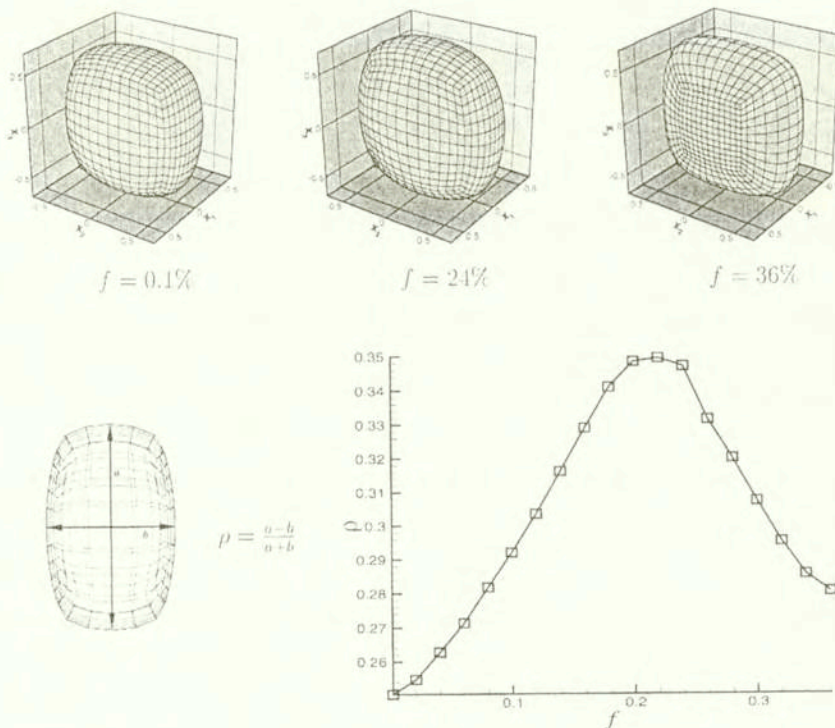
$\rho = \dfrac{a-b}{a+b}$

FIG. 9. Equilibrium shapes under external loading for different volume fractions f.

Expressing the external load by equivalent eigenstrains leads to higher values for the eigenstrain tensor in x_1-direction. If the inclusion is assumed to be soft compared to the matrix material, an oblate particle shape minimizes the dominant energy $E^{el,out}$ with the x_1-axis being normal to the flat face of the particle. An increasing volume fraction supports this effect, therefore ρ increases, until a volume fraction $f = 25\%$ is reached. Even higher values of the volume fraction f lead to large deformations of the matrix material in the regions where $\partial \mathcal{B}$ and Γ are close together, which in turn cause higher values of $E^{el,out}$. This energy can be reduced if the distance between the matrix and the particle boundary is increased, so smaller values for ρ are the consequence. The occurrence of oblate particle shapes in tensile loading is called rafting. It has a great technical relevance as the rafting process alters the general elastic behaviour of the considered structure.

5. Conclusions

The theory of equilibrium shapes in two-phase materials has been recast for a periodic cell arrangement. A variational principle was used to derive necessary conditions for an equilibrium shape. Material parameters that resemble Ni-base alloys were used in the simulation with Boundary Elements. The influence of some important parameters on the equilibrium shape was discovered by parameter studies. Although not the complete physically relevant parameter range was analyzed, some conclusions can be drawn:

- With increasing particle size the equilibrium shape becomes more cube-like. This is in agreement with results for the isolated particle.

- In the case of no applied loads, increasing the volume fraction makes the equilibrium shape more spheroidal as long as the volume fraction is lower than $40 - 50\%$. Above this critical volume fraction, the particle becomes again more cuboidal. Thus up to volume fractions of about $10 - 15\%$, the particle interaction is not relevant for the equilibrium shape.

- For reasonable stiffness ratios of particle to matrix material, the characteristic behaviour is not altered drastically.

- In the case of applied loads, the rafting tendency increases with increasing particle interaction until a volume fraction of about 25%. Increasing the volume fraction further leads to less oblate shapes. However, in this regime particle coalescence which was neglected in this analysis, might become relevant.

References

1. M. IGNAT, J.-Y. BUFFIERE and J. M. CHAIX, *Microstructures induced by a stress gradient in a nickel-based superalloy*, Acta Metall. Mater., **41**, 3, 855–862, 1993.

2. J. LI, R. WAHI, H. CHEN, W. CHEN and H. WEVER, *Deformation substructure in the nickel-base alloy in 738lc under superimposed creep-fatigue loading*, Z. Metallkd., **84**, 4, 268–272, 1993.

3. T. M. POLLOCK and A. S. ARGON, *Directional coarsening in nickel-base single crystals with high volume fractions of coherent precipitates*, Acta Metall. Mater., **43**, 6, 1859–1874, 1994.

4. M. FAHRMANN, W. HERMANN, E. FAHRMANN, A. BOEGLI, T. M. POLLOCK and H. G. SOCKEL, *Determination of matrix and precipitate elastic constants in* $(\gamma - \gamma')$ *Ni-base model alloys, and their relevance to rafting*, Materials Science and Engineering, **A 260**, 212–221, 1999.

5. J. W. CAHN, *On spinodal decomposition*, Acta Metall., **9**, 795–801, 1961.

6. J. W. CAHN and J. E. HILLARD, *Spinondal decomposition: A reprise*, Acta Metall., **19**, 151–161, 1971.

7. P. H. LEO and R. F. SEKERKA, *The effect of surface stress on crystal-melt and crystal-crystal equilibrium*, Acta Metall., **37**, 12, 3119–3138, 1989.

8. M. E. GURTIN and P. W. VOORHEES, *The continuum mechanics of coherent two-phase elastic solids with mass transport*, Proc. R. Soc. Lond., A **440**, 323–343, 1993.

9. M. E. GURTIN, *The nature of configurational forces*, Arch. Rational Mech. Anal., **131**, 67–100, 1995.

10. M. E. GURTIN and P. W. VOORHEES, *The thermodynamics of evolving interfaces far from equilibrium*, Acta Mater., **44**, 1, 235–247, 1996.

11. G. A. MAUGIN, *Material Inhomogeneities in Elasticity*, Chapman and Hall, London, Glasgow, New York, Tokyo, Melbourne, Madras 1993.

12. E. FRIED and M. E. GURTIN, *Continnum theory of thermally induced phase transitions based on an order parameter*, Physica D, **68**, 326–343, 1993.

13. E. FRIED and M. E. GURTIN, *Dynamic solid-solid transitions with phase characterized by an order parameter*, Physica D, **72**, 287–308, 1994.

14. J. K. LEE, *Coherency strain analysis via discrete atom method*, Scr. Met. Mat., **32**, 4, 559–564, 1995.

15. J. K. LEE, *Effects of applied stress on coherent precipitates via a disctrete atom method*, Metals and Materials, **2**, 3, 183–193, 1996.

16. J. K. LEE, *A study on coherency strain precipitate morphology via a discrete atom method*, Met. Mat. Trans., **27A**, 1449–1459, 1996.

17. J. K. LEE, *Morphology of coherent precipitates via a discrete atom method*, Mat. Sci., **A238**, 1–12, 1997.

18. S. KOLLING and D. GROSS, *Description of two–phase materials using discrete atom method*, ZAMM, 2000 (to appear).

19. J. K. LEE, *Elastic stress and microstructural evolution*, Materials Transactions, JIM, **39**, 1, 114–132, 1998.

20. A. G. KHACHATURYAN, *Theory of Structural Transformation in Solids*, John Wiley and Sons, 1983.

21. T. KÜPPER and N. MASBAUM, *Simulation of particle growth and Ostwald ripening via the Cahn-Hilliard equation*, Acta Metall. Mater., **42**, 6, 1847–1858, 1994.

22. P. H. LEO, J. S. LOWENGRUB and H. J. JOU, *A diffuse interface model for microstructural evolution in elastically stressed solids*, Acta Mater., **46**, 6, 2113–2130, 1998.

23. Y. WANG, L.-Q. CHEN and A. G. KHACHATURYAN, *Kinetics of strain-induced morphological transformation in cubic alloys with a miscibility gap*, Acta Metall. Mater., **41**, 1, 279–296, 1993.

24. J. D. ZHANG, D. Y. LI and L. Q. CHEN, *Shape evolution and splitting of a single coherent particle*, Mat. Res. Soc. Symp. Proc., **481**, 243–248, 1998.

25. Y. WANG, L.-Q. CHEN and A. G. KHACHATURYAN, *Three-dimensional dynamic calculation of the equilibrium shape of a coherent tetragonal precipitate in mg-partially stabilized cubic ZrO_2*, J. Am. Ceram. Soc., **79**, 4, 967–991, 1996.

26. P. W. VOORHEES, G. B. MCFADDEN and W. C. JOHNSON, *On the morphological development of second-phase particles in elastically-stressed solids*, Acta Metall. Mater., **40**, 11, 2979–2992, 1992.

27. M. E. THOMPSON, C. S. SU and P. W. VOORHEES, *The equilibrium shape of a misfitting precipitate*, Acta Metall. Mater., **42**, 6, 2107–2122, 1993.

28. C. H. SU and P. W. VOORHEES, *The dynamics of precipitate evolution in elastically stressed solids – I, inverse coarsening*, Acta Mater., **44**, 5, 1987–1999, 1996.

29. C. H. SU and P. W. VOORHEES, *The dynamics of precipitate evolution in elastically stressed solids – II, particle alignment*, Acta Mater., **44**, 5, 2001–2016, 1996.

30. I. SCHMIDT and D. GROSS, *A strategy for determining the equilibrium shape of an inclusion*, Arch. Mech., **47**, 2, 379–390, 1995.

31. I. SCHMIDT and D. GROSS, *The equilibrium shape of an elastically inhomogeneous inclusion*, J. Mech. Phys. Solids, **45**, 9, 1521–1549, 1997.

32. I. SCHMIDT, R. MUELLER and D. GROSS, *The effect of elastic inhomogeneity on equilibrium and stability of a two particle morphology*, Mechanics of Materials, **30**, 181–196, 1998.

33. R. MUELLER and D. GROSS, *3D simulation of equilibrium morphologies of precipitates*, Comp. Mat. Sci., **11**, 35–44, 1998.

34. R. MUELLER and D. GROSS, *3D inhomogeneous, misfitting second phase particles – equilibrium shapes and morphological development*, Comp. Mat. Sci., **16**, 53–60, 1999.

35. A. J. ARDELL and P. K. RASTOGI, *The coarsening behaviour of the γ' precipitate in Nickel-Silicon alloys*, Acta Metall., **19**, 321–330, 1971.

36. A. J. ARDELL and A. MAHESHWARI, *Anomalous coarsening behaviour of small volume fractions of Ni_3Al precipitates in binary Ni-Al alloys*, Acta Metall. Mater., **40**, 10, 2661–2667, 1992.

37. A. J. ARDELL and M. MESHKINPOUR, *Role of volume fraction in the coarsening of Ni_3Si precipitates in binary Ni-Si alloys*, Material Science and Engineering, **A 185**, 153–163, 1994.

38. T. MURA, *Micromechanics of Defects in Solids*, Martinus Nijhoff Publishers, 1987.

39. I. SCHMID and D. GROSS, *Directional coarsening in Ni-base superalloys: analytical results for an elasticity based model*, Proc. R. Soc. Lond., **455**, 3085–3106, 1999.

40. J. D. ESHELBY, *Energy relations and the energy-momentum tensor in continuum mechanics*, 77–115, McGraw Hill, New York 1970.

41. W. C. JOHNSON and J. W. CAHN, *Elastically induced shape bifurcations of inclusions*, Acta Metall., **32**, 11, 1925–1933, 1984.

42. W. C. JOHNSON, M. B. BERKENPAS and J. W. CAHN, *Precipitate shape transitions during coarsening under uniaxial stress*, Acta Metall., **36**, 2, 3149–3162, 1988.

43. I. M. KAGANOVA and R. L. ROITBURD, *Equilibrium between elastically-interacting phases*, Sov. Phys. JETP, **67**, 4, 1173–1183, 1988.

44. D. G. LUENBERGER, *Linear and nonlinear programming*, Addison-Wesley, 2nd ed. 1984.

45. C. A. BREBBIA and J. F. C. TELLES, *Boundary Element Techniques*, Springer-Verlag, 1985.

46. N. A. SCHCLAR, *Anisotropic Analysis using Boundary Elements*, [In:] Topics in Engineering, **20**, Computational Mechanics Publications, Southampton UK and Boston USA 1994.

47. D. J. BACON, D. M. BARNETT and R. O. SCATTERGOOD, *Anisotropic continuum theory of lattice defects*, Progress in Materials Science, **23**, 55–262, 1979.